manuscript submitted to *Journal of Geophysical Research: Planets*

Wang, Y., Zhuo, M., Wu, B., Liu, S., & Guo, D. (2025). Automatic classification of primary and secondary craters near Copernicus crater with updated insights on its impact trajectory and age. Journal of Geophysical Research: Planets, 130, e2024JE008516. To view the published open abstract, go to http://dx.doi.org/10.1029/2024JE008516.

Automatic Classification of Primary and Secondary Craters near Copernicus Crater with Updated Insights on Its Impact Trajectory and Age

Yiran Wang[1]*, Miao Zhuo[1], Bo Wu[2]*, Shuo Liu[2], Dijun Guo[3]

[1] Department of Earth and Space Sciences, Southern University of Science and Technology, Shenzhen, Guangdong, China

[2] Research Centre for Deep Space Explorations | Department of Land Surveying & Geo-Informatics, The Hong Kong Polytechnic University, Hung Hom, Kowloon, Hong Kong

[3] State Key Laboratory of Space Weather, National Space Science Center, Chinese Academy of Sciences, Beijing, 100190, China

Corresponding author: Yiran Wang (wangyr@sustech.edu.cn), Bo Wu (bo.wu@polyu.edu.hk)

Key Points:

- A catalog of 324,000 primary and secondary craters with diameters ≥200 m is established in and around the Copernicus crater.
- A deep learning method was developed to classify primary and secondary craters near the Copernicus crater using spectral features.
- Copernicus crater is ~755 Ma and overlays a ~3.69 Ga surface, with secondary craters suggesting a southeast-to-northwest impact trajectory.

Abstract

Impact cratering is the dominant geological process shaping the Moon's surface. Primary craters form from direct asteroid or comet impacts, while secondary craters are created by debris ejected from these primary impacts. Accurately identifying secondary craters within the primary crater population is essential for understanding planetary processes and surface ages. However, manually distinguishing these secondary craters can be time-consuming and challenging. In this work, a statistical analysis of 5,460 primary and secondary craters reveals significant differences in their spectral characteristics. These differences are postulated to originate from distinct degrees of modification to the target materials and weathering processes. Employing a deep learning model, the research specifically targets the Copernicus crater region to automate the identification of secondary craters. The model classified ~285,000 secondary and ~39,000 primary craters with diameters from 200 m to 5 km. Secondary craters make up 89% of the total at 200-280 m, decreasing to around 65% at 4520-5000 m. The azimuthal distribution of identified secondary craters suggests an oblique impact from southeast to northwest that formed the Copernicus crater. The model age, based on craters superposed on the ejecta, estimates the Copernicus crater to be ~ 755 Ma, overlaying a 3.69 Ga surface. The estimated ages aligns with previous research. The method is best suited for geologically homogeneous, airless surfaces, and is limited when older primary craters are buried by later ejecta or when ancient craters exhibit similar spectral features due to degradation.

Plain Language Summary

The Moon's surface is marked by numerous craters that provide valuable insights into its geological history and are widely used for determining surface ages and reconstructing impact events. Direct impacts from asteroids or comets that form primary craters can excavate very large cohesive fragments, leading to the formation of numerous secondary craters as the debris falls back to the surface. Studying impact craters to decipher planetary processes and surface ages of bodies requires the identification of secondary craters among the population of primary craters. This study introduces a novel method that uses spectral analysis to distinguish between the two types of craters. A deep learning model was applied to automate crater identification and classification around the Copernicus crater, efficiently categorizing approximately 285,000 secondary and 39,000 primary craters. This technique also provided insights into the formation of the Copernicus crater, suggesting an oblique impact from the southeast, and supported model age estimates of 755 million years, aligning with previous geological data. The method is best suited for geologically homogeneous, airless surfaces, and is limited when older primary craters are buried by later ejecta or when ancient craters exhibit similar spectral features due to degradation.

1 Introduction

Impact craters represent the most prominent geomorphological features on the Moon. Their number, type, and distribution serve as valuable records of geomorphological evolution and geological events. Primary craters originate from direct impacts of celestial bodies, while secondary craters result from fragments ejected during primary impacts.

Figure 1 illustrates the formation of secondary craters. From the rim of the primary crater outward, there is a zone with continuous ejecta deposit, followed by a region characterized by continuous secondaries facies. This area is marked by numerous chained and clustered secondary

craters that are consistently distributed along the radial direction. Beyond this region lies the discontinuous secondaries facies. Most secondary craters within discontinuous secondaries facies are typical secondary crater chains that exhibit intermittent radial distribution, like those found within distant ejecta rays. Some of the secondary craters located within the discontinuous secondary facies tend to be more sporadically distributed and lack distinct characteristics. They feature circular crater rims, dispersed spatial distribution, and morphologies identical to primary craters. Those secondary craters cannot be directly identified by relying solely on shape and distribution characteristics, hence termed background secondary craters. (Bierhaus et al., 2018; McEwen and Bierhaus, 2006; Wilhelms et al., 1978; Xiao, 2018; Xiao et al., 2014).

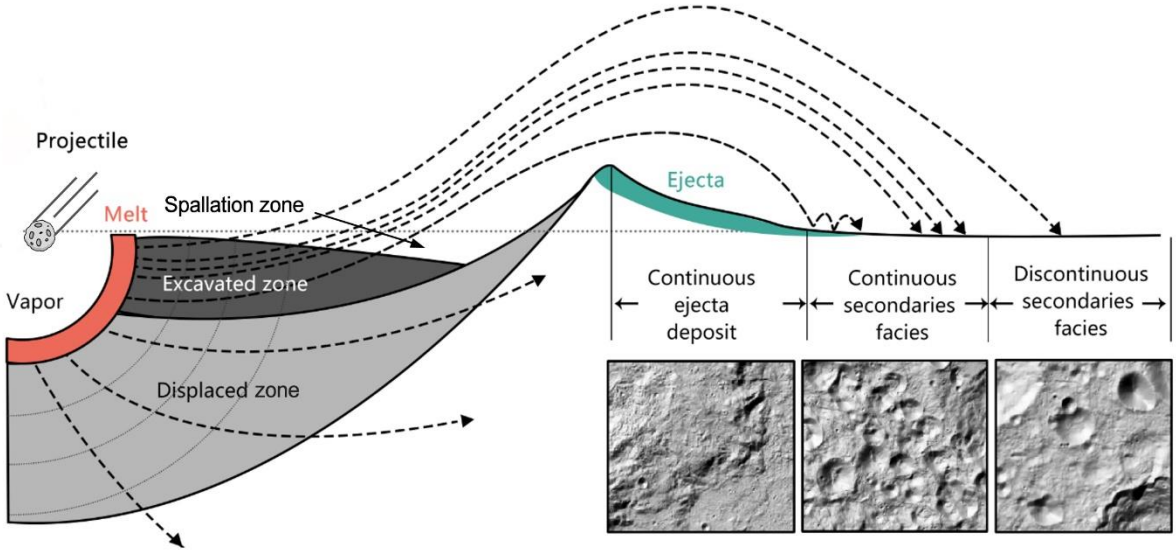

Figure 1. Schematic diagram of the impact excavation process to form secondary craters, adapted from Osinski et al. (2011) and Xiao et al. (2014).

The identification of secondary craters is crucial in understanding impact processes and history. These craters provide valuable insights into reconstructing impact scenarios, including parameters like impact angle and velocity (e.g., Herrick and Forsberg-Taylor, 2003; Herrick & Hessen, 2006; Singer et al., 2020). Secondary craters also offer valuable insights into the age of their associated primary crater (Lagain et al., 2021a) and reveal characteristics of the target surface (Robbins & Hynek, 2014; Lagain et al., 2021b).

Moreover, the influence of secondary craters on age dating remains controversial. Statistical analysis of the crater size-frequency distribution (CSFD) of impact craters helps delineate geological units and estimate their model ages (Ivanov, 2001; Neukum et al., 2001). The fundamental assumption of the commonly used CSFD age estimation method (e.g., Neukum et al., 2001) is that impact craters are randomly accumulated. This assumption ignores spatial and temporal variations of the impact flux and impact conditions (essentially angle and speed) due to the Moon's orbit characteristics around the Earth and the source of impactors (Le Feuvre and Wieczorek, 2011; Lagain et al., 2024; Wang and Zhou, 2016). Consequently, regions with older surface ages are expected to have more impact craters. Based on this fundamental

assumption, the impact craters involved in the statistical analysis should exclusively include primary craters. Theoretically, accurate model age estimation requires excluding secondary craters, including both chain-like and background types resembling primary craters. However, crater counting and production functions on which crater-derived age techniques are based remove chain-like features, avoid ejecta zones, or focus on only large craters (e.g., Neukum et al., 1975; 2001) but often include background secondary craters. As smaller craters (<1 km) are included in CSFD analyses (e.g., Greeley and Gault, 1970), background secondary craters inevitably influence the dating results. McEwen and Bierhaus (2006) noted that the secondaries might be a problem for production functions. However, Hartmann and Daubar (2017) believe that primary crater plus background secondaries offered the best proxy for estimating chronometric information. The impact of background secondary craters on model age estimation remains a subject of ongoing debate (e.g., Bierhaus et al., 2018; McEwen et al., 2005; Xiao and Strom, 2012; Hartmann et al., 2010).

The identification of typical secondary craters is primarily accomplished through expert manual annotation based on their experience. This process relies on the morphological and distribution characteristics of secondary craters (e.g., Guo et al., 2018; Robbins and Hynek, 2014) in visible data, as depicted in Figure 2: (a) they are distributed in a chain or "V" shape, with the arms of the "V" oriented toward the main primary crater; (b) they occur in clusters and have steeper CSFD in certain diameters; and (c) they are elliptical with their long axis pointing towards the center of the main primary crater, or in other irregular shapes. However, identification process is highly subjective, as there is no consensus on the criteria of "irregular", "chains" and "clusters". In addition, while elliptical or irregular shapes can occasionally result from primary impacts, elliptical primary craters formed by low-angle impacts (<~12°) are rare, accounting for only ~4% of cases (Gault and Wedekind, 1978; Bottke et al., 2000; Kenkmann and Poelchau, 2009), making clustered elliptical primaries unlikely.

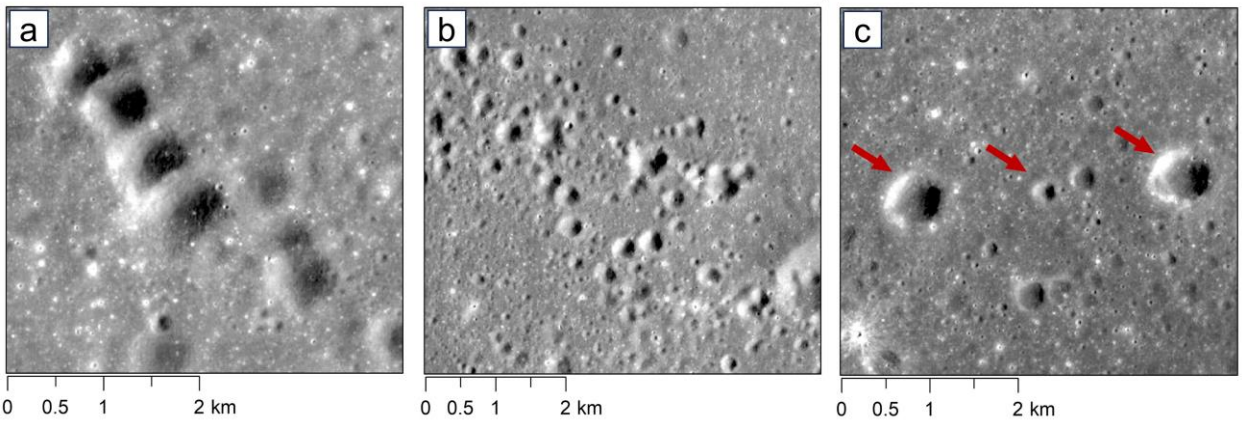

Figure 2. Morphological and distribution characteristics of secondary craters are presented in visible images. (a) chain-like distribution (TCO_MAP_02_N09E345N06E348SC), (b) cluster-like distribution (TCO_MAP_02_N06E330N03E333SC), and (c) irregular shape (TCO_MAP_02_N00E336S03E339SC).

To distinguish secondary craters, scholars have introduced various methods. Kumar et al. (2011) observed that craters with central mound tend to result from low-velocity impacts,

making this feature a potential indicator of secondary craters. However, low-velocity impacts are not the exclusive mechanism responsible for central mound formation, and this method is limited to a specific diameter range. Nagumo and Nakamura (2001), through statistical analysis, proposed that if the ratio of the long axis to the short axis of an elliptical impact crater exceeds 1.2, the crater can be suggested as a secondary crater. Yet this approach is not definitive, as high-velocity, low-angle impacts can also produce elliptical craters (Bottke et al. 2000). Bart and Melosh (2007) compared the distribution of rocks around craters of similar size and found that secondary craters typically have larger surrounding boulders, reflecting the lower energy of their formation. However, this method relies heavily on high-resolution imagery and manual identification, limiting its practical application.

Subsequent studies applied cluster analysis techniques to identify secondary craters (Kreslavsky, 2007; Michael et al., 2012; Salih et al., 2017; Lagain et al., 2021c). For instance, Salih et al. (2017) used Monte Carlo simulations and Voronoi tessellation to detect impact craters, leveraging the principle that primary craters follow a random distribution, whereas secondary craters tend to cluster. Similarly, Lagain et al. (2021c) adopted the method by Andronov et al. (2016) to exclude likely secondary crater clusters by identifying deviations from expected random distributions. Such cluster-based methods are limited when applied to areas dominated by crater clusters, within individual clusters, in very small areas, or to regions with too few craters (Lagain et al. 2021c). More recently, Cao et al. (2022) applied a multiwavelet approach to characterize topographic variations within craters and their ejecta, establishing threshold values that help distinguish secondaries from primaries of similar size and age. However, this method is constrained by the resolution of elevation data and is also limited to specific diameter ranges.

Relying solely on visible imagery and digital elevation models (DEMs) presents challenges in distinguishing between primary and secondary craters. Introducing spectral information can offer additional insights, as differences in composition and weathering can influence reflectance properties. In the following, we explore these two factors to clarify their role in separating primary and secondary craters.

Differences in composition are one of the factors contributing to variations in reflectance spectra between primary and secondary craters. These differences arise from the contrasting impact velocities during crater formation. Primary craters are formed by meteorite hypervelocity impacts with sufficient impact energy to produce initial shock waves with velocities above the speed of sound. Ivanov (2001) and Le Feuvre and Wieczorek (2011) estimated the average impact velocities of asteroids on the Moon to be 16 $km.s^{-1}$ and 19.7 $km.s^{-1}$, respectively. Yue et al. (2013) simulated the orbital evolution of main-belt asteroids and determined that 75% of lunar impact velocities exceed 12 $km.s^{-1}$. Wang and Zhou (2016) further estimated typical impact speeds of 25.5 $km.s^{-1}$ from main-belt asteroids and 22.3 $km.s^{-1}$ from near-Earth objects. The velocity of secondary crater-forming spallation is limited by the escape velocity of the object, which is about 2.4 $km.s^{-1}$ for the Moon (McEwen & Bierhaus, 2006). These high-energy impacts allow primary craters to access deeper layers, resulting in ejecta with distinct compositional properties. In contrast, secondary craters, even those of similar size, lack the energy to excavate such materials, leading to clear compositional differences.

The degree of weathering also influences the differences in reflectance spectra. Secondary craters formed during a single impact event exhibit uniform weathering levels, provided they form within the same geological unit, with minimal topographic variation, and on

airless bodies. However, nearby primary craters often vary in age, resulting in a broader range of weathering conditions. Additionally, the deeper penetration of primary impacts also penetrates deeper into the lunar crust, exposing and ejecting materials that have undergone less surface exposure and space weathering, compared to the regolith typically redistributed by secondary impacts.

In summary, primary craters, formed by high-energy impacts, excavate deeper, less weathered, and potentially more competent materials, when located within the same geological unit. In contrast, secondary impacts that generate craters of similar size lack the energy to reach such depths. Due to differences in formation times, they also experience varying degrees of weathering. These differences in composition and weathering can be detected in spectral data, resulting in observable spectral contrasts between secondary and surrounding primary craters. However, such distinctions are more apparent in relatively young regions. In older areas, long-term space weathering and surface mixing tend to obscure these variations. Although the precise age limit is unclear, Hawke et al. (2004) suggest that compositional features can persist for over 1.1 billion years, implying detectable spectral differences in younger terrains. Therefore, we selected a relatively young region, the Copernicus impact crater area, as our study area.

The differences between primary and secondary craters in reflectance spectral data have not been addressed in previous studies. Consequently, the reflectance spectral data have not been fully utilized in identifying secondary craters. In this study, the research area and data were outlined in Section 2. In Section 3, a novel approach for identifying secondary craters on the lunar surface using reflectance spectral data and deep learning is developed and evaluated. The approach is then implemented in the study area, and the results of primary and secondary crater classification are presented and analyzed in Section 4, which provides extended analyses and comparisons. Sections 5 and 6 present the discussion and conclusion.

2 The Study Area and Spectral Data

2.1 Dataset

Owing to the launch and operation of several recent lunar missions, remote-sensing spectral data of favorable spatial resolution have become available, offering the possibility for automatic differentiation of secondary craters, particularly those under 1 km in diameter. This research adopted the reflectance spectral data acquired by the Multiband Imager (MI) of the Selenological and Engineering Explorer (SELENE) mission. The SELENE MI acquired data in nine ultraviolet-visible spectroscopy (UVVIS; 415, 750, 900, 950, and 1001 nm) and near-infrared (NIR; 1000, 1050, 1250, and 1550 nm) spectral bands. The instrument provides a spatial resolution of ~20 m in the UVVIS, and ~60 m in the NIR at the nominal altitude of 100 km (Haruyamaet al., 2008; Ohtake et al., 2009). In addition to the reflectance spectral data, orthoimage mosaics derived from SELENE Terrain Camera (TC) images were also used, with spatial resolutions better than 10 m/pixel (Kato et al., 2008).

SELENE TC imagery and SELENE MI data exhibit certain geospatial discrepancies, ranging from 10 to 50 meters within the experimental region. A manual registration process was employed, utilizing SELENE TC imagery as the georeferencing reference.

2.2 Copernicus Crater

The study area focuses on the Copernicus crater and its ejecta blanket. Copernicus crater is a notable crater on the lunar surface with a prominent ray system and distinguishable secondary chains. The Copernicus crater (with a central coordinate of 9.62°N, 20.08°W) and its surrounding regions were selected as the study area in this research, as depicted in Figure 3. It is a well-developed complex crater with a raised rim, well-formed terraces, an extensive melt-covered floor, and central peaks. Figure 3a displays the SLDEM color map, where red denotes higher elevation, and blue represents lower elevation. Figure 3b presents visible light imagery of the area, showcasing the extensive, high-reflectance ejecta rays that extend across nearby mare and overlay ejecta from other craters.

The Copernicus crater played a pivotal role in the early studies of the Moon's stratigraphy. Over fifty years ago, lunar geologists Shoemaker and Hackman (1962) used the Copernicus crater to establish the basic stratigraphy of the lunar surface. Later, material believed to be ejecta from Copernicus was collected by Apollo 12 astronauts. Radiometric dating of these samples indicated an age of approximately 800 Ma (Alexander et al., 1976; Bogard et al., 1994; Eberhardt et al., 1973; Meyer Jr et al., 1971; Silver, 1971; Stöffler and Ryder, 2001). Subsequent studies have employed crater counting methods to estimate the model age of Copernicus crater. Hiesinger et al. (2012) conducted manual crater counts in three ejecta regions, obtaining an age of ~797 Ma. Fairweather et al. (2023) subsequently refined these counting areas and implemented a semi-automated approach, revising the age estimate to 860 Ma. Meanwhile, Terada et al. (2020) performed manual counts in floor, ejecta, and central peak melt regions, reporting a younger age of 660 Ma.

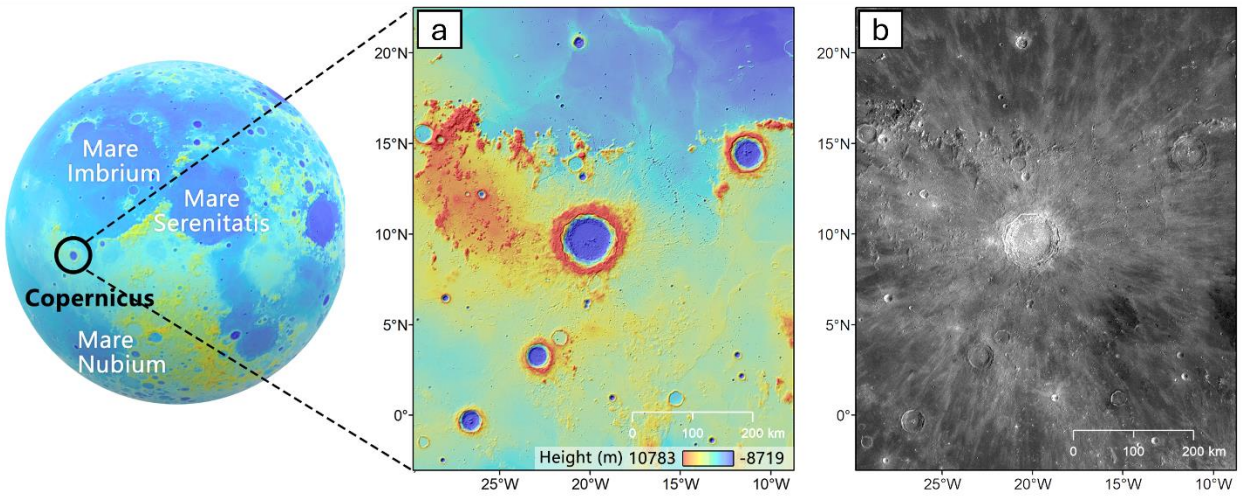

Figure 3. The Copernicus crater and its surrounding regions. (a) SLDEM color map overlaid onto a hill-shade rendering of SLDEM and (b) SELENE TC image.

3. Automatic Detection of Secondary Craters Based on Deep Learning

3.1 Overview of the Approach

The overall architecture of the proposed approach for automatically classifying secondary craters from spectral data is illustrated in Figure 4. The process begins with the manual

identification of primary and secondary craters based on their characteristic morphological features. Next, the corresponding spectral data of the manually identified craters are extracted to create training samples, and the spectral differences between primary and secondary craters are analyzed. Following this, a deep learning approach is applied for classification. During the training phase, a subset of the labeled MI training samples is used to train a modified deep learning model, resulting in a classifier capable of distinguishing secondary craters based on spectral input. Finally, crater detection is performed in the Copernicus region, and the classifier is applied to classify all detected craters as primary or secondary.

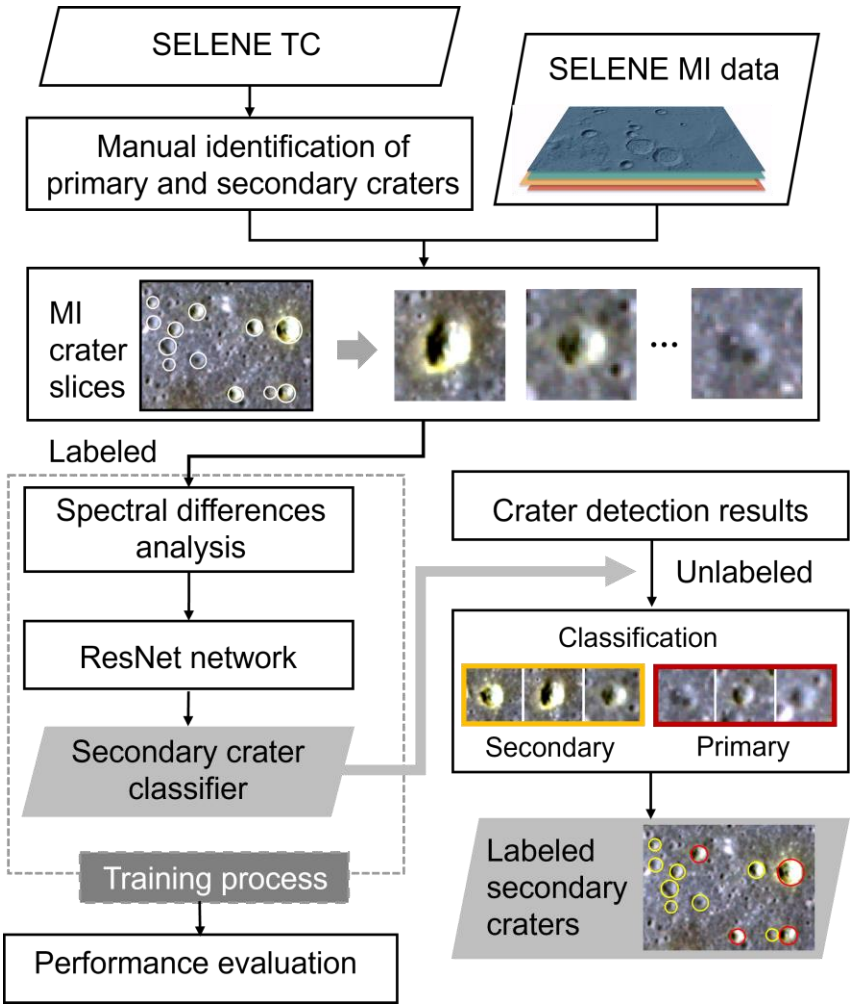

Figure 4. Framework of the proposed approach for classification of secondary craters on spectral data.

3.2 Manual Identification of Primary and Secondary Craters

The classification process begins with the manual identification of primary and secondary craters based on their characteristic morphological features. A total of 2,112 primary craters and 3,363 secondary craters were manually labeled using the SELENE TC mosaic across five regions. It should be noted that the manual annotations do not cover all craters within the area.

Craters lacking distinct morphological or distribution characteristics were not classified as either primary or secondary.

As Figure 5a shows, the primary craters (marked in cyan) are craters with regular circle rims, isolated distribution, or bright radiant patterns, while the secondary craters (marked in yellow) are craters in chains, in groups, or in elliptical shapes. Given the subjective nature of primary and secondary crater identification, the mentioned criteria cannot ensure flawless classification. Nevertheless, they are statistically reliable, with the majority of identifications being accurate. The cumulative crater frequency of the manually labeled craters is plotted in Figure 5b. To validate that the identified secondary craters exhibit morphological characteristics consistent with a secondary origin, and to quantitatively assess differences in crater morphology, depth-to-diameter (d/D) ratios were compared between primary and secondary craters. The results are provided in Text S1 of the Supplementary Information. For manually labeled craters larger than 400 m in diameter around the Copernicus crater, the mean d/D value is 0.136 for primary craters and 0.087 for secondary craters.

All labeled craters were used to create the training and validation datasets for the classification of secondary craters. The craters in the five regions are subdivided into two groups. The area outlined by the white rectangle is designated for validation, containing 819 primary craters and 1,459 secondary craters. The remaining area, which includes 1,293 primary craters and 1,904 secondary craters, is allocated for model training. Craters of various sizes were cropped from the MI data and resized to a uniform size (i.e., 64×64 pixels in this research), which is suitable for revealing both the crater and its surrounding features and is optimal for deep learning models.

To expand the training dataset and improve the model's ability to generalize, the cropped training samples were augmented using rotational and flipping techniques. This process increased the diversity of the dataset, resulting in 11,424 secondary crater samples and 7,758 primary crater samples. These augmented samples were then used to analyze spectral differences between primary and secondary craters and were subsequently fed into the deep learning network for classification.

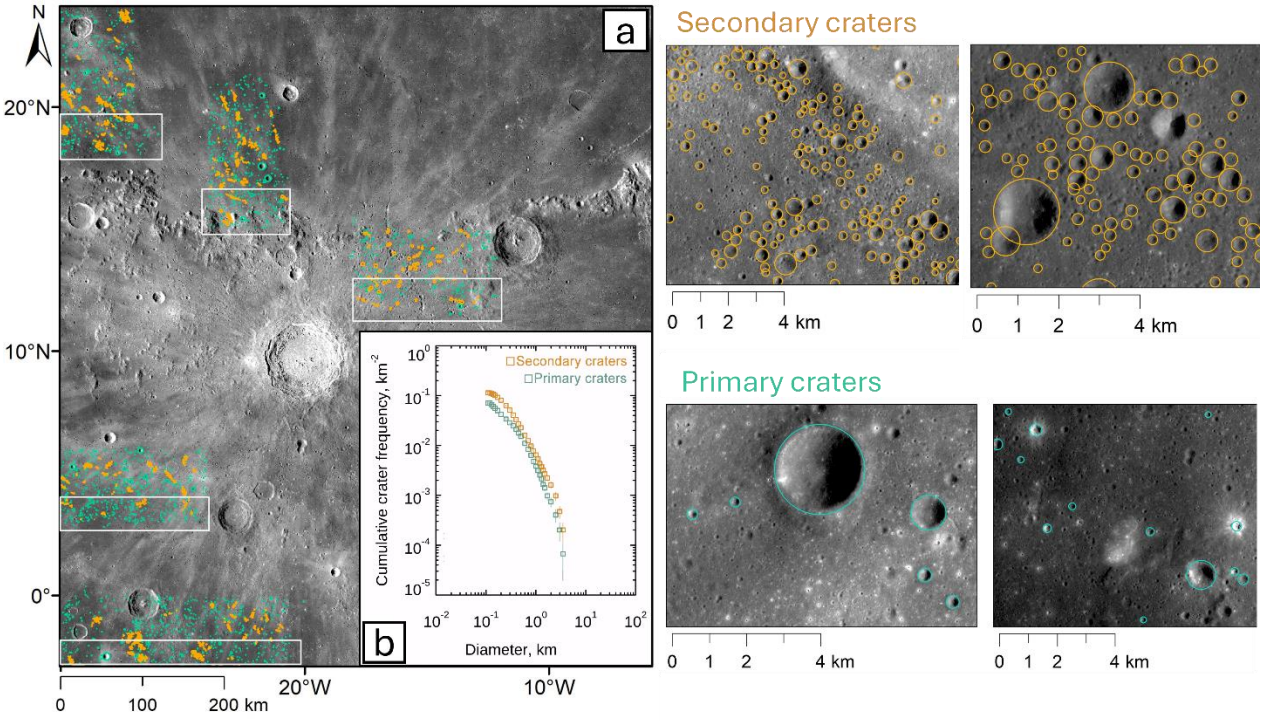

Figure 5. (a) Manually identified primary and secondary craters along with illustrative examples. (b) Cumulative crater frequency of the manually identified primary and secondary. Note that not all craters in the area were annotated; those without clear morphological or distribution features were not classified as either primary or secondary craters.

3.4 Training Sample Determination and Spectral Differences Analysis

The reflectance spectral differences between primary and secondary craters are the basis for the automatic secondary crater classification approach proposed in this research. For the 2,112 manually labeled primary craters and 3,363 secondary craters, a buffer zone was created by extending outward from the crater rim by a distance equal to the crater's diameter (as illustrated in Figure 6), which primarily encompasses the continuous ejecta deposits. The crater area and its buffered zone were subdivided into six regions along the radial direction, as illustrated in Figure 6. The average value of reflectance spectral data in band 1 (415 nm) was calculated for each section at the corresponding location, denoted as A1 to F1, respectively (as illustrated in Figure 6). The same calculations were applied to the remaining eight bands as well.

The average spectral values were computed for all manually labeled primary and secondary craters, and they are depicted in a box-and-whisker plot in Figure 7. The box lines indicate the minimum, first quartile, median, third quartile, and maximum values, respectively. The horizontal coordinates are the 1-9 bands of the multispectral data, the vertical coordinates are the average reflectance value of SELENE MI data, and the colors of the box lines correspond to the positions marked in Figure 6. As can be seen from Figure 7, there are significant differences between the primary and secondary craters in all 9 bands: the spectral value of the primary crater is significantly higher than that of the secondary crater in all 9 bands; the box of

the primary crater decreases from inside the crater to outside the crater, while the secondary crater shows a slight increase trend; the spectral value of the primary craters takes on a wider range of values than that of the secondary craters.

The underlying causes of the observed spectral differences remain unclear. However, it is likely that surface composition and the degree of space weathering are the primary influencing factors. High-energy primary impacts may excavate more subsurface bedrock, exposing less-weathered material both within the crater and in the ejecta. These materials generally exhibit higher reflectance values. This likely explains the spectral pattern in Figure 7, where primary craters show higher reflectance than secondary craters. The distribution of fragmented bedrock gradually diminishes from the crater rim outward, accounting for the gradual decrease in reflectance observed from the rim of primary craters, as also shown in Figure 7.

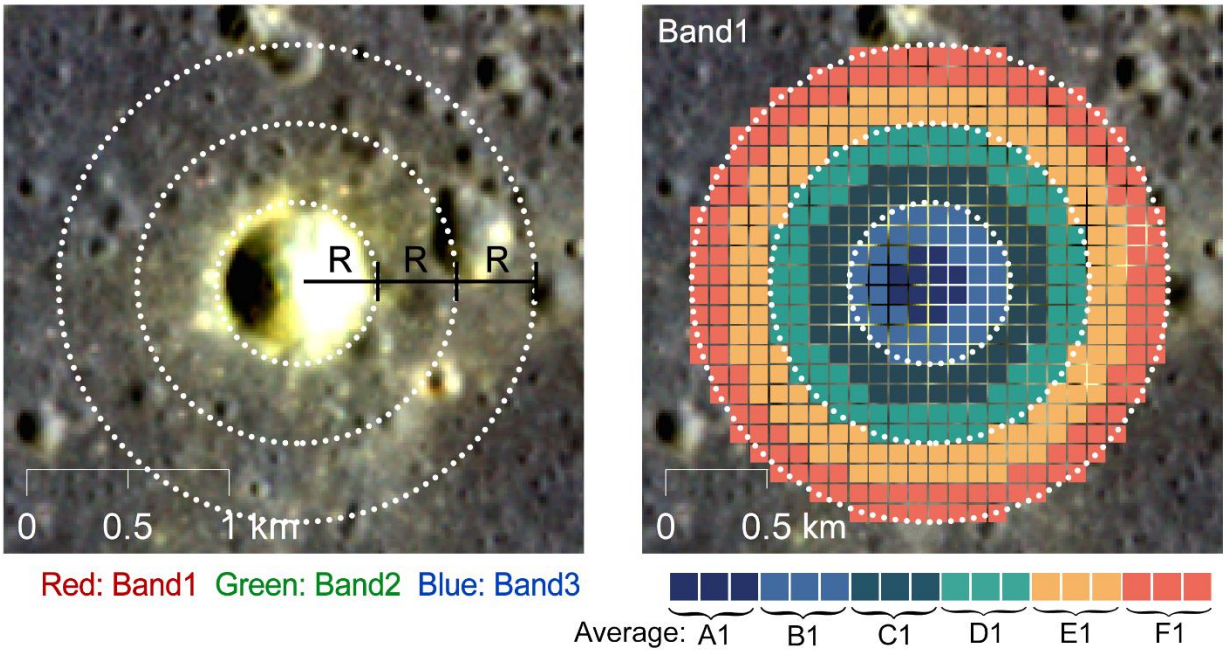

Figure 6. The schematic diagram illustrates expanding a diameter-sized buffer zone outward from the crater rim and dividing this area into six regions. The average reflectance spectral value is calculated for each region.

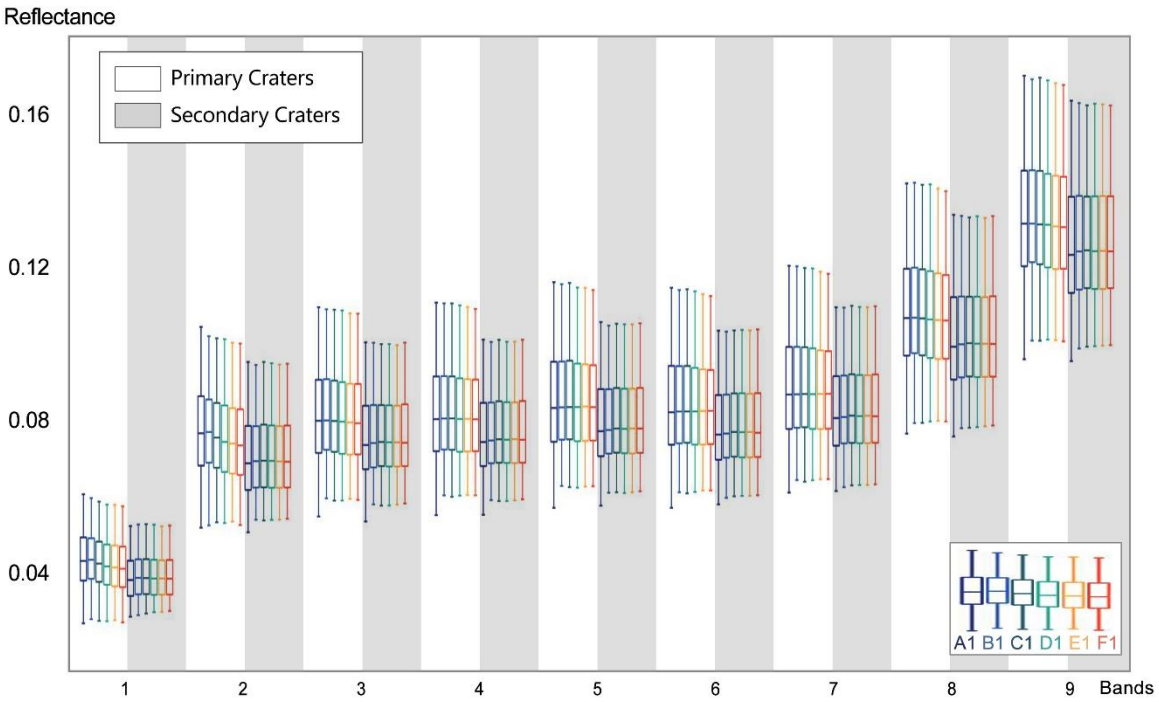

Figure 7. Box-and-whisker plot of the average reflectance spectral values of the subregions for primary craters (with white background) and secondary craters (with gray background). The x-axis is the 9 bands of the SELENE MI data, and the y-axis is the average value of SELENE MI data. For each band, the whisker represents the minimum and maximum of all of the data while the upper quartile, median, and lower quartile are marked by the box. The six different colors correspond to different colored regions from the innermost to the outermost, as illustrated in Figure 6.

3.5 Deep-Learning Approach for Secondary Crater Classification

The observed spectral differences between primary and secondary craters form the basis for training a deep learning model to automate secondary crater classification. Using the manually labeled dataset, we trained a convolutional neural network to distinguish between the two crater types. The shapefile used for training the classification of primary and secondary craters is publicly accessible at Zhuo and Wang (2024). The classification model is based on ResNet-50, a deep convolutional neural network belongs to the ResNet family, developed by Microsoft Research (He et al., 2016). ResNet-50 consists of 50 layers and incorporates residual connections, which allow information to bypass certain layers. These connections help prevent the vanishing gradient problem and enable the model to learn more effectively from deeper architectures. The network is built from residual blocks, each containing convolutional layers, batch normalization, and ReLU activation functions. This structure allows the model to capture complex spatial and spectral patterns within the input data. Due to its proven performance in image classification tasks (Sharma et al., 2022), ResNet-50 was selected as the backbone network for identifying secondary craters from spectral data.

The structure of the adopted ResNet-50 network for secondary crater classification is shown in Figure 8. The first layer in the modified ResNet-50 network is the convolution layer with an input size of (64 × 64 × 9), where 64 × 64 is the size of the input MI crater patches, and 9 is the number of multispectral bands for the MI data. This layer convolves the input with a filter of size of 3 × 3 and provides an output with 64 feature maps of size of 32 × 32 × 64. The maximum pooling layer forms the second layer, which sub-samples the output of the first layer with a pooling size of 3 × 3 and gives an output of 16 × 16 with 64 feature maps. After the initial layers, the network architecture incorporates four large residual blocks, constituting the core of the neural network. Each residual block follows a standardized structure: initially, a 1×1 convolution kernel is employed for dimensionality reduction, followed by a 3×3 kernel for spatial convolution, concluding with another 1×1 kernel to upscale the dimensions. Throughout this process, the output of each residual block is fused with the input that has undergone a direct dimensionality upscaling, thereby integrating features effectively. Specifically, after the first residual block, the spatial dimensions of the image remain unchanged, while the depth of the feature map increases from 64 to 256. In each subsequent block, the depth of the feature map first reduces to half and then quadruples, concurrently with a gradual halving of the spatial dimensions. Finally, the network converges these features through a global average pooling layer followed by a fully connected layer, setting the stage for the classification task. The network culminates with a softmax layer comprising two neurons designated for distinguishing between primary and secondary craters.

Notably, there were substantial variations in the values across the 9 bands of MI data. To enhance the convergence speed of the network, a normalization process was applied to each band, adjusting the values of each band to a range of 0 to 1.

During the training process, the approach employs the cross-entropy (De Boer et al., 2005) function as the loss function and utilizes a stochastic gradient descent optimizer (LeCun et al., 1989) during training. To prevent overfitting, weight decay is incorporated as a regularization technique, with the weight decay value set to 0.008. A unique training strategy called "freezing training" is implemented. In the initial 2 epochs, the training exclusively focuses on the weights of the classifier, using a batch size of 32. Subsequently, from the 3rd to the 12th epoch, the training encompasses all model weights, and the batch size is adjusted to 16. This gradual unfreezing and training approach aims to optimize efficiency throughout the training process, thereby enhancing the overall performance of the model.

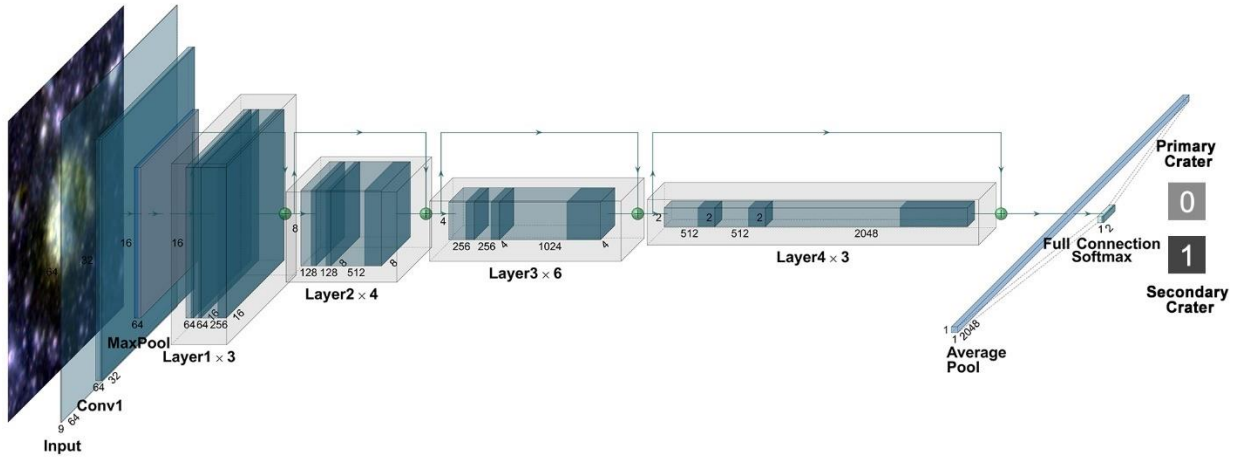

Figure 8. The structure of the modified ResNet-50 network for the classification of the secondary craters.

3.6 Performance Evaluation

For a quantitative evaluation, the numbers of true positive (TP, correctly labeled secondary craters), true negative (TN, correctly labeled primary craters), false positive (FP, incorrectly classified secondary craters), and false negative (FN, incorrectly classified primary craters) of the 2278 labeled craters for evaluation are listed in Table 1. The overall performance is evaluated using precision, recall, and accuracy metrics, yielding values of 94.96%, 93.00%, and 92.36%, respectively. The detailed calculations are presented in Table 1. Examples of the evaluation results are presented in Figure 9. It is worth noting that the relatively high accuracy is attributed to the fact that these test samples consist of only manually labeled, representative primary and secondary craters, rather than covering all craters within the study area. Craters without clear distinguishing features could not be confidently classified by human experts into either category, therefore were not included in the evaluation dataset. The evaluation results are illustrated in Figure 9, and the performance metrics are detailed below. The shapefile used for validating the classification of primary and secondary craters is publicly accessible at Zhuo and Wang (2024).

$$Precision = \frac{TP}{TP+FP} = 94.96\% \quad (1)$$

$$Recall = \frac{TP}{TP+FN} = 93.00\% \quad (2)$$

$$Accuracy = \frac{TP+TN}{TP+TN+FP+FN} = 92.36\% \quad (3)$$

Table 1. Evaluation results of the secondary crater classification approach based on craters exhibiting distinct secondary and primary morphological features.

Datasets	Diameter (m)	TP	FP	FN	TN	Precision (%)	Recall (%)	Accuracy (%)
SELENE TC	≥200	758	56	86	425	93.12	89.81	89.28
	≥400	266	24	42	201	91.72	86.36	87.62
	≥800	69	10	9	53	87.34	88.46	86.52

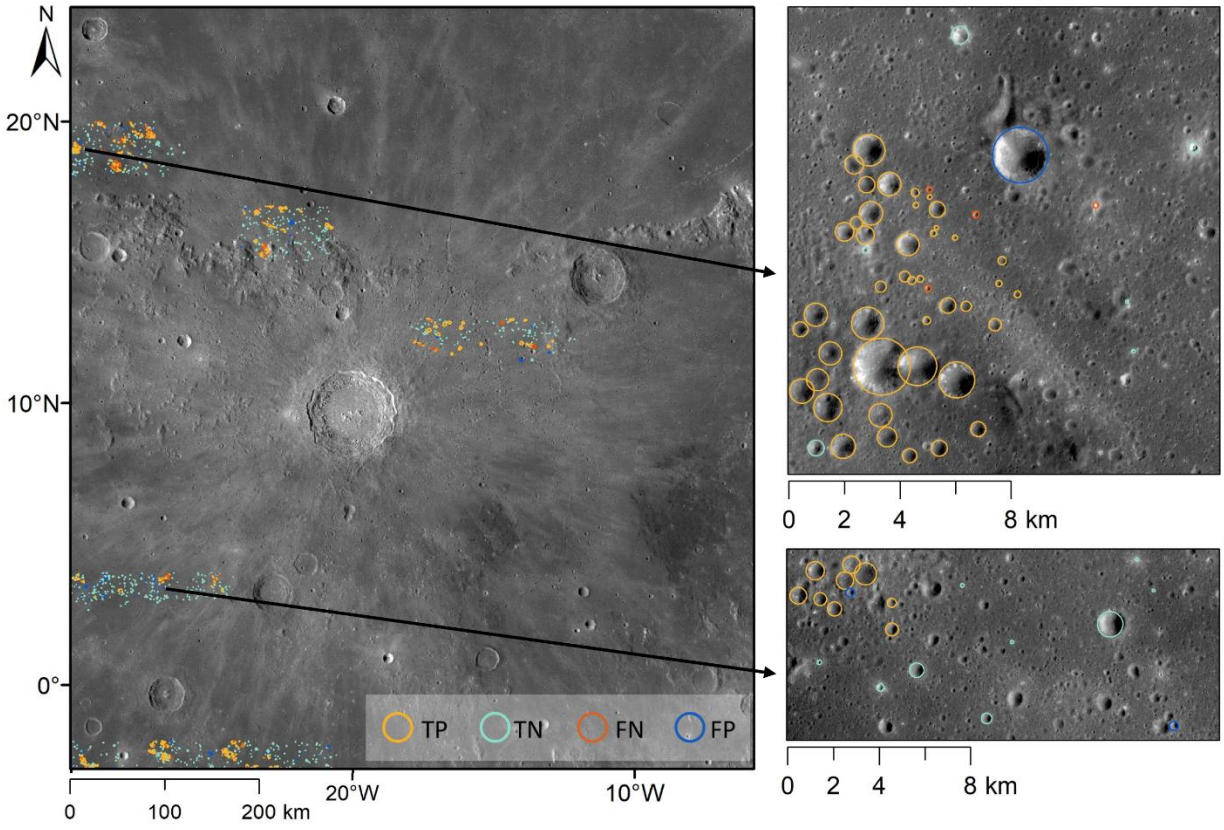

Figure 9. Examples of the evaluation results. Yellow, cyan, red, and blue represent TP, TN, FN, and FP, respectively. Note that the evaluation is conducted only on craters exhibiting distinct secondary or primary morphological features.

4. Secondary Craters around the Copernicus Crater

4.1 Crater Extraction from SELENE TC Images

In this study, the proposed automated classification approach was applied to identify secondary craters around the Copernicus Crater. The first step in this process involves accurately locating crater positions before classification can occur. Crater detection was performed using an open-source Automatic Crater Detection (ACD) tool (Wang et al., 2024), which is described in detail by Zhuo et al. (2025). The tool incorporates active learning, enabling continuous improvement by adding challenging samples from diverse landforms, ultimately creating a training set of 55,504 samples for the Moon (Zhuo et al., 2025). This approach enables reliable crater detection across complex planetary surfaces, with a minimum detectable diameter of 10 pixels. Quantitative evaluations of the crater detection on SELENE TC data show high performance, with Precision (reliability of detections) of 92.5%, Recall (detection rate) of 96.6%, and F1 score (harmonic mean of Precision and Recall) of 94.5% (Zhuo et al., 2025). Further evaluation conducted in the study area yielded F1 scores of 93.8% for craters larger than 200

meters and 93.1% for craters larger than 400 meters. Detailed metrics can be found in Text S2 of the Supplementary Information. The evaluation dataset has also been made available. These results are comparable to recent deep learning-based crater detection methods (e.g., Fairweather et al., 2022,2023; Lagain et al., 2021c; Benedix et al., 2020).

Based on the automatic results, a subsequent manual review and digitization process was carried out using SELENE TC images, involving the removal of 4,793 artifacts and the addition of 1,885 previously missed craters. Details of the manual refinement are provided in Text S3 of the Supporting Information. In total, approximately 324,000 craters with diameters ranging from 200 m to 5 km were identified and cataloged, as shown in Figure 10a.

The density of craters was measured in moving windows with a 5 km radius and 200 m step, as shown in Figure 10b. In and around the Copernicus crater, there is a radial area of low density, which is believed to be the region covered by ejecta during the formation of the impact crater. The ejecta has overlaid the originally existing impact craters, and due to the Copernicus crater being relatively young, there is less accumulation of new impact craters in the ejecta.

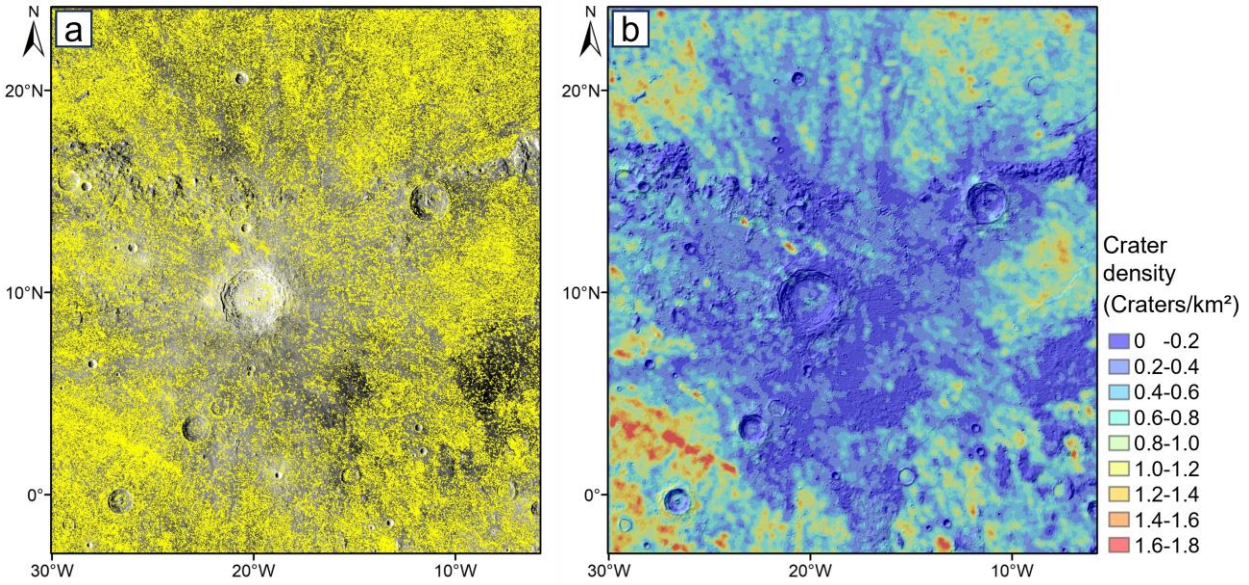

Figure 10. (a) Crater catalog covering the regions in and around the Copernicus crater. (b) Crater density maps in the study area are calculated in moving windows of a 5 km radius. The unit for crater density is given as crater numbers per square kilometer.

4.2 Classification of Primary and Secondary Craters around the Copernicus Crater

Utilizing the crater catalog in and around the Copernicus crater as a basis, the corresponding MI data are cut into small patches and fed into the pre-trained secondary crater identification model. This process enables the classification of all 324,000 craters into primary and secondary categories. 285,000 were classified as secondary craters (Figure 11a), and 39,000 as primary craters (Figure 11c). The classification results align with the morphological and distribution patterns of primary and secondary craters. For instance, craters categorized as secondary often exhibit a chain-like distribution (e.g., Figure 11b), while those classified as

primary display distinct ejecta rays, a more circular shape, or a relatively isolated distribution (e.g., Figure 11d).

It is worth noting that craters larger than 5 km (approximately 5% of the Copernicus crater diameter) were excluded from the classification, as previous research indicates that the secondary-to-primary diameter ratio is less than 2-5% on planetary surfaces (Lagain et al., 2021a; 2021b; Robbins and Hynek, 2014; Schultz and Singer, 1980; Shoemaker et al., 1970). Moreover, the classification of such large craters would be unreliable, as the training dataset does not include examples of craters larger than 5 km in diameter. Larger craters also exhibit different excavation processes and weathering rates compared with smaller ones, which further limits the model's applicability to these cases.

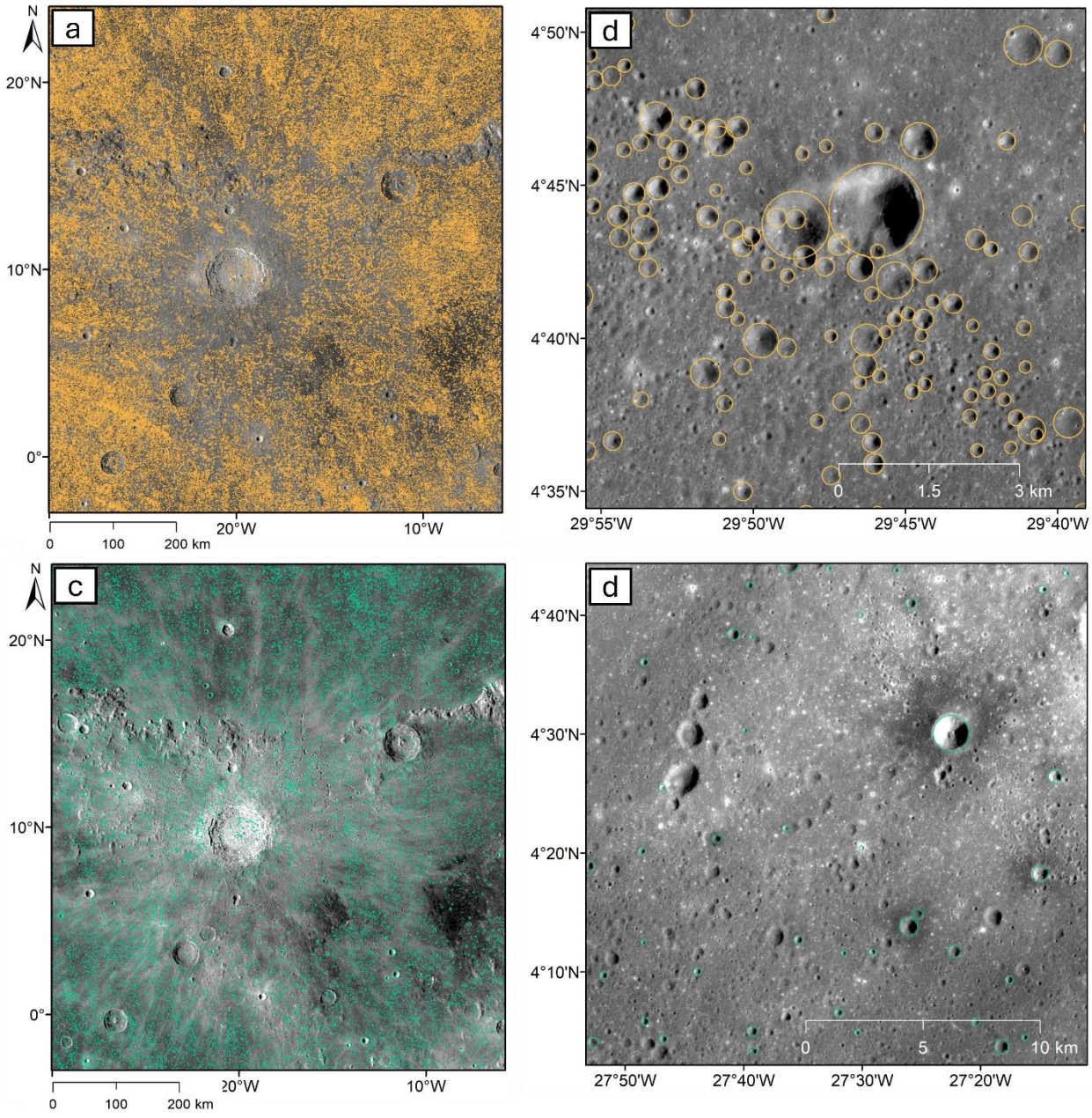

Figure 11. Classification results of (a) secondary craters and (c) primary craters in and around the Copernicus crater. Examples of a magnified region illustrate (b) craters classified as secondary exhibiting a chain-like distribution and (d) craters classified as primary display distinct ejecta rays, a more circular shape, or a relatively isolated distribution. Background image is SELENE TC image with a resolution of 10 m.

Table 2 lists the quantity and percentage distribution of primary and secondary craters across different diameter ranges. The proportion of secondary craters accounts for almost 90% of relatively small craters (200–400 m), and this percentage decreases to ~60% with the increasing diameter of impact craters. Apart from a small portion of classified secondary craters with distinct morphological and distribution characteristics, most of them seem to be background secondaries, with discrete distribution and have similar morphological characteristics to primary craters. Existing studies are polarized on the issue of the proportion of background secondary craters in the overall crater population. One view is that the proportion of background secondary craters in the overall population is less than 10% (Neukum and Ivanov, 1994; Neukum et al., 1975). However, opponents argue that the proportion of background secondary craters is much greater, with the vast majority of impact craters less than 1 km in diameter being background secondary craters (Dundas and McEwen, 2007; Xiao et al., 2014). The statistics presented in Table 2 reveal that secondary craters account for 80%-90%. The proportion of secondary craters decreases with increasing diameter but still exceeds half.

Table 2. The number and proportion of primary and secondary craters across different diameter ranges.

Diameter	Primary Crater Count	Secondary Crater Count	Secondary Crater Ratio
200-280 m	11,736	96,355	89.14%
280-400 m	14,398	113,161	88.71%
400-560 m	6,101	38,950	86.46%
560-800 m	3,841	22,558	85.45%
800-1130 m	1,634	7,730	82.55%
1130-1600 m	818	4,068	83.26%
1600-2260 m	306	1,433	82.40%
2260-3200 m	143	640	81.74%
3200-4520 m	52	159	75.36%
4520-5000 m	9	17	65.38%

5. Discussion

5.1 Azimuthal Distribution of Secondary Craters

The azimuthal distribution analysis of secondary craters was conducted in the area within a radius of 180 km outside the Copernicus crater (gray areas in Figure 12a), as depicted in Figure 13a. This region was chosen to avoid the prominently visible chain of secondary craters in the southwest direction originating from other impact craters. Secondary crater chains potentially associated with Kepler and Aristarchus craters, located to the west and northwest of Copernicus, as well as from unknown sources, are marked in Figure 12a. Figure 12b presents a rose diagram illustrating the distribution of secondary craters. These craters are categorized into azimuthal sectors, each spanning 22.5°. The length of each sector corresponds to the number of secondary craters within that specific azimuthal range, with different colors indicating various crater diameter ranges. The marked crater chains were excluded from the calculation, and the missing directional areas were normalized to ensure an accurate representation. This rose diagram highlights notable variations across different azimuths.

Ejecta planforms can be broadly categorized into five types: symmetric, offset, offset and concentrated cross range, forbidden zone, and butterfly, ranging from near-vertical to low-angle incidence impact (Guo et al., 2018; Herrick and Forsberg-Taylor, 2003; Herrick a Hessen, 2006). The distribution pattern of secondary craters around the Copernicus crater appears to align with the characteristics of the “offset” planform, as shown in Figure 12c. The southwest (~225°–270°) shows high density, while the southeast (~135°–180°) shows low density. It is interpreted that the Copernicus crater may be caused by an oblique impact from southeast to northwest.

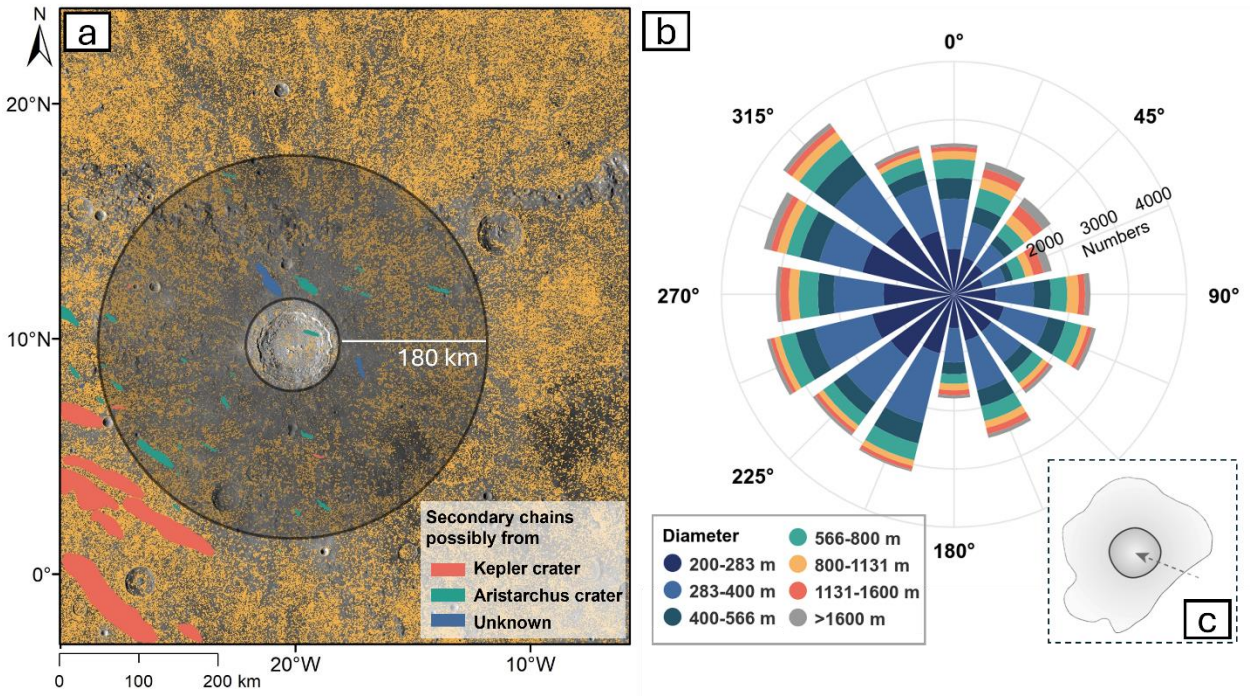

Figure 12. (a) The study areas for azimuthal distribution analysis. Secondary crater chains potentially associated with Kepler and Aristarchus craters, located to the west and northwest of

Copernicus, are marked in red and green. (b) Azimuthal distribution of secondary craters around the Copernicus crater. Each bar represents a 22.5° azimuthal wide sector. The color of the bar represents a certain number of craters with a specific range of diameters. (c) "offset" ejecta planform based on (Guo et al., 2018). The implied direction of impact is shown by the arrow.

5.2 Age Estimation of the Copernicus Crater

Crater counts provide a foundation for determining model-dependent absolute ages of planetary surfaces. Absolute surface ages are derived from CSFD, which relies on established chronology models. In this research, we use the CraterStats software (Michael and Neukom, 2010) to align the measured CSFD with production function by Neukum et al., (2001), using fitting technique of least-squares regression. By correlating the CSFD with the calibrated chronology functions, absolute surface ages can be derived.

Theoretically, crater-based dating should only account for primary craters. However, secondary craters, particularly background secondary craters, were inherently included in the design of the original dating curves (e.g., Neukum et al., 2001). Consequently, when performing age estimations, it is generally sufficient to exclude regions with obvious secondary craters without explicitly addressing the background secondary crater population. To evaluate the influence of background secondary craters, we conducted age estimations for the Copernicus crater using two different approaches.

The first approach performs age estimation for the Copernicus crater by the classified primary craters superposed to the Copernicus crater cavity or within its ejecta areas. The boundary of the Copernicus crater ejecta was defined using the Geologic Map of the Moon (Fortezzo et al., 2020), while the interior boundary of the crater was manually delineated, as shown in Figure 13a. The model ages were estimated to be 607 Ma and 712 Ma, based on craters superposed to the Copernicus crater cavity and its ejecta, respectively, as illustrated in Figure 13b.

In the second approach, we followed conventional methods by excluding regions with obvious secondary craters and performed CSFD-based dating using all remaining craters within the counting area (Figure 13c). In the Copernicus ejecta region, these craters may either be overprinted (pre-existing craters, as discussed in Fairweather et al. 2023) or superposed by the ejecta. Only the latter subset (superposed craters) contributes to determining the model age of the Copernicus crater. The pre-existing craters, being larger and less likely to be buried, led to a noticeable gap in the CSFD plot between crater diameters of approximately 1 km and 3 km (Figure 13d). The age estimation for the main counting region was divided into two parts: (1) craters superposed on the Copernicus ejecta yield a model age of 755 Ma, representing the formation age of the Copernicus crater; (2) larger craters, including pre-Copernicus ones, suggest an older surface age of 3.69 Ga. Additionally, craters superposed to the Copernicus crater cavity produced an estimated model age of 986 Ma, as shown in Figure 13b. Completeness analyses (Robbins et al., 2018) for the craters used in this approach are provided in Text S4 and illustrated in Figure S4.

The radiometric age of Copernicus crater is 800 Ma according to the samples from Apollo 12 (Alexander et al., 1976; Bogard et al., 1994; Eberhardt et al., 1973; Meyer Jr et al., 1971; Silver, 1971; Stöffler and Ryder, 2001) and the estimated model ages by other research are ~660 Ma (Terada et al., 2020), 779 Ma (Hiesinger et al., 2012) and 860 Ma (Fairweather et al.,

2023) based on CSFD. According to the radiometric age, the age (755 Ma) estimation derived from the ejecta blanket, excluding regions with obvious secondary craters, is the closest. Removing background secondary craters may lead to an underestimation of the age. Furthermore, age estimation using ejecta blanket regions and within the crater cavity inherently carries uncertainties, as the distinct terrain properties of ejecta blankets can influence crater morphology, thereby biasing age estimates derived from crater statistics (e.g., Kirchoff and Marchi, 2019; Kirchoff et al., 2021; Marchi et al., 2011, Williams et al., 2018). This introduces potential errors in the age estimations of this study. However, no standardized or reliable correction method currently exists to address this issue (Kirchoff et al., 2021).

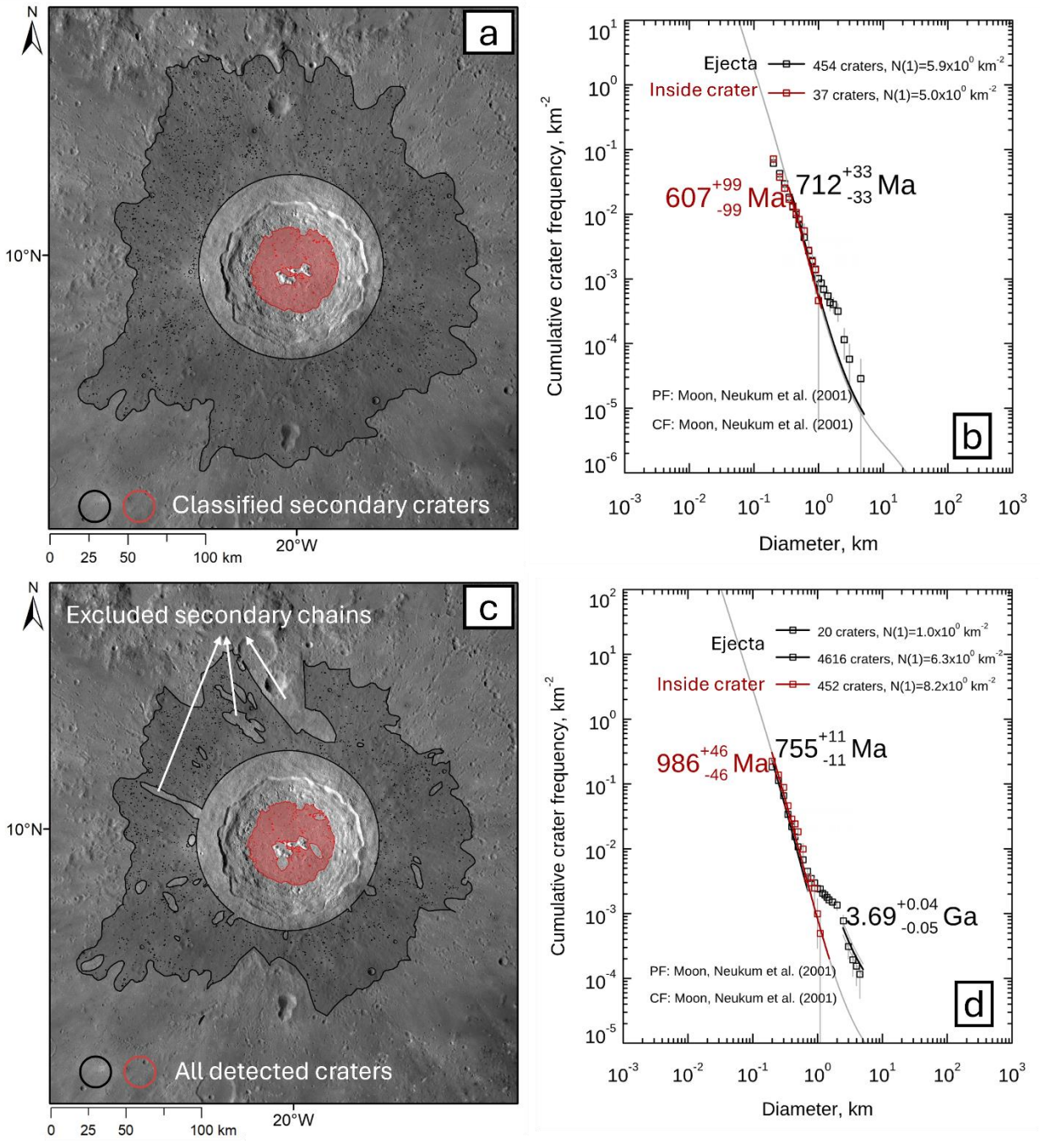

Figure 13. (a) Classified primary craters superposed to the Copernicus crater cavity and its ejecta blanket, used for model age estimation. (b) CSFD and estimated model ages based on the classified primary craters shown in (a). (c) Detected craters superposed to the Copernicus crater cavity and ejecta blanket, excluding regions dominated by secondary crater chains, utilized for refined model age estimation. (d) CSFD and model age estimates based on the craters in (c).

6. Conclusion

We have developed an automated approach for identifying secondary craters based on reflectance spectral data, achieving an accuracy of 92% based on manually labeled craters with distinct secondary/primary features. This method facilitated the creation of a catalog containing approximately 324,000 craters with diameters ranging from 200 m to 5 km, encompassing the Copernicus crater and its surroundings. Key findings from this new crater catalog include:

- Spectral data analysis highlights clear distinctions between primary and secondary craters surrounding the Copernicus crater, drawing from 2,112 manually identified primary craters and 3,363 secondary craters. These differences are postulated to originate from variations in the extent of alterations to the target materials and surface weathering.
- Secondary craters, predominantly background secondaries, constitute around 89% at 200-280 m in diameter, decreasing to approximately 65% when craters gradually increase to 4520-5000 m in diameter in the study area.
- The azimuthal distribution of secondary craters suggests that the Copernicus crater may have resulted from an oblique impact from southeast to northwest.
- Copernicus crater is estimated to be ~755 Ma overlaying ~3.69 Ga surface, based on CSFD analysis of craters superposed to ejecta. The removal of background secondary craters would lead to an underestimation of the age.

Classifying primary and secondary craters using reflectance spectral data remains challenging, particularly when older primary craters are covered by ejecta from other impacts, or when craters on more ancient surfaces have faded into similar spectral features. Such overlap can introduce bias into surface age estimates, underscoring the need for future research to better characterize and mitigate this effect. Additionally, this method is most effective on geologically homogeneous, airless surfaces, where spectral contrasts are more pronounced. The distinction between primary and secondary craters also involves inherent subjectivity, and the method's performance in regions like Copernicus crater has yet to be rigorously quantified.

Despite these limitations, this research represents our first attempt to use spectra to distinguish between primary and secondary craters, aiming to provide insights for future studies.

Acknowledgments

We want to thank Dr. Anthony Lagain for his valuable feedback during the review process of this study. We acknowledge the LRO and Kaguya mission teams for providing the orbital data. This work was supported by a grant from the National Natural Science Foundation

of China (42201424) and a grant from the Research Grants Council of Hong Kong (RIF Project No: R5043-19).

Data Availability Statement

To support further research, the following datasets are publicly available in Zhuo and Wang (2024): (1) crater detection evaluation data, (2) shapefiles for crater classification training and evaluation, (3) catalog of primary and secondary craters in and around Copernicus Crater, and (4) source data for age estimation.

References

Alexander, E. C., Bates, A., Coscio Jr, M., Dragon, J., Murthy, V., Pepin, R. O., & Venkatesan, T. (1976). K/Ar dating of lunar soils II. In: Pergamon Press.

Andronov, L., Orlov, I., Lutz, Y., Vonesch, J.L. and Klaholz, B.P. (2016). ClusterViSu, a method for clustering of protein complexes by Voronoi tessellation in super-resolution microscopy. Scientific reports, 6(1), p.24084. doi: 10.1038/srep24084.

Bart, G. D., & Melosh, H. (2007). Using lunar boulders to distinguish primary from distant secondary impact craters. Geophysical research letters, 34(7). doi: 10.1029/2007GL029306.

Benedix, G.K., Lagain, A., Chai, K., Meka, S., Anderson, S., Norman, C., Bland, P.A., Paxman, J., Towner, M.C. and Tan, T., (2020). Deriving surface ages on Mars using automated crater counting. Earth and Space Science, 7, e2019EA001005. doi: 10.1029/2019EA001005.

Bierhaus, E., McEwen, A. S., Robbins, S., Singer, K., Dones, L., Kirchoff, M., & Williams, J. P. (2018). Secondary craters and ejecta across the solar system: Populations and effects on impact-crater–based chronologies. Meteoritics & Planetary Science, 53(4), 638-671. doi: 10.1111/maps.13057.

Bogard, D., Garrison, D., Shih, C., & Nyquist, L. (1994). 39Ar-40Ar dating of two lunar granites: The age of Copernicus. Geochimica et Cosmochimica Acta, 58(14), 3093-3100. doi: 10.1016/0016-7037(94)90181-3.

Bottke WF Jr, Love SG, Tytell D, Glotch T (2000) Interpreting the elliptical crater populations on Mars, Venus, and the Moon. Icarus 145:108-121. doi: 10.1006/icar.1999.6323.

Cao, W., Xiao, Z., Xu, R., & Wang, Y. (2022). Extracting Background Secondary Craters Based on Fusion of Multiscale and Multifacies Crater Topography Information. IEEE Transactions on Geoscience and Remote Sensing, 60, 1-16. doi: 10.1109/TGRS.2022.3195201.

De Boer, P.-T., Kroese, D. P., Mannor, S., & Rubinstein, R. Y. (2005). A tutorial on the cross-entropy method. Annals of operations research, 134, 19-67. doi: 10.1007/s10479-005-5724-z.

Dundas, C. M., & McEwen, A. S. (2007). Rays and secondary craters of Tycho. Icarus, 186(1), 31-40. doi: 10.1016/j.icarus.2006.08.011.

Eberhardt, P., Geiss, J., Grögler, N., & Stettler, A. (1973). How old is the crater Copernicus? The Moon, 8(1), 104-114. doi: 10.1007/BF00562752.

Fairweather, J. H., Lagain, A., Servis, K., Benedix, G. K., Kumar, S. S., & Bland, P. A. (2022). Automatic mapping of small lunar impact craters using LRO-NAC images. Earth and Space Science, 9, e2021EA002177. doi:10.1029/2021EA002177

Fairweather, J.H., Lagain, A., Servis, K. and Benedix, G.K. (2023). Lunar surface model age derivation: Comparisons between automatic and human crater counting using LRO-NAC and Kaguya TC images. Earth and Space Science, 10(7), p.e2023EA002865. doi: 10.1029/2023EA002865.

Fortezzo, C., Spudis, P., & Harrel, S. (2020). Release of the digital unified global geologic map of the Moon at 1: 5,000,000-Scale. Paper presented at the 51st Annual Lunar and Planetary Science Conference. https://www.hou.usra.edu/meetings/lpsc2020/pdf/2760.pdf

Greeley, R. and Gault, D.E., (1970). Precision size-frequency distributions of craters for 12 selected areas of the lunar surface. The Moon, 2(1), pp.10-77. doi: 10.1007/BF00561875.

Guo, D., Liu, J., Head III, J. W., & Kreslavsky, M. (2018). Lunar Orientale impact basin secondary craters: Spatial distribution, size-frequency distribution, and estimation of fragment size. Journal of Geophysical Research: Planets, 123(6), 1344-1367. doi: 10.1029/2017JE005446.

Hartmann, W.K. and Daubar, I.J. (2017). Martian cratering 11. Utilizing decameter scale crater populations to study Martian history. Meteoritics & Planetary Science, 52(3), pp.493-510. doi: 10.1111/maps.12807.

Hartmann, W.K., Quantin, C., Werner, S.C. and Popova, O. (2010). Do young martian ray craters have ages consistent with the crater count system?. Icarus, 208(2), pp.621-635. doi: 10.1016/j.icarus.2010.03.030.

Haruyama, J., Hara, S., Hioki, K., Iwasaki, A., Morota, T., Ohtake, M., et al. (2012). Lunar global digital terrain model dataset produced from SELENE (Kaguya) terrain camera stereo observations. Paper presented at the 43rd Annual Lunar and Planetary Science Conference. https://www.lpi.usra.edu/meetings/lpsc2012/pdf/1200.pdf

Haruyama, J., Matsunaga, T., Ohtake, M., Morota, T., Honda, C., Yokota, Y., et al. (2008). Global lunar-surface mapping experiment using the Lunar Imager/Spectrometer on SELENE. Earth, planets and space, 60(4), 243-255. doi: 10.1186/BF03352788.

Hawke, B.R., Blewett, D.T., Lucey, P.G., Smith, G.A., Bell III, J.F., Campbell, B.A. and Robinson, M.S. (2004). The origin of lunar crater rays. Icarus, 170(1), pp.1-16. doi: 10.1016/j.icarus.2004.02.013.

He, K., Zhang, X., Ren, S., & Sun, J. (2016). Deep residual learning for image recognition. Paper presented at the Proceedings of the IEEE conference on computer vision and pattern recognition. doi: 10.1109/CVPR.2016.90.

Herrick, R. R., & Forsberg-Taylor, N. K. (2003). The shape and appearance of craters formed by oblique impact on the Moon and Venus. Meteoritics & Planetary Science, 38(11), 1551-1578. doi: 10.1111/j.1945-5100.2003.tb00001.x.

Herrick, R. R., & Hessen, K. K. (2006). The planforms of low-angle impact craters in the northern hemisphere of Mars. Meteoritics & Planetary Science, 41(10), 1483-1495. doi: 10.1111/j.1945-5100.2006.tb00431.x.

Hiesinger, H.V., Van Der Bogert, C.H., Pasckert, J.H., Funcke, L., Giacomini, L., Ostrach, L.R. and Robinson, M.S. (2012). How old are young lunar craters?. Journal of Geophysical Research: Planets, 117(E12). doi: 10.1029/2011JE003935.

Ivanov, B. A. (2001). Mars/Moon cratering rate ratio estimates. Space Science Reviews, 96(1-4), 87-104. doi: 10.1007/978-94-017-1035-0_4.

Kreslavsky, M.A. (2007) July. Statistical characterization of spatial distribution of impact craters: Implications to present-day cratering rate on Mars. In Seventh international conference on mars, Vol. 1353, p. 3325. https://www.lpi.usra.edu/meetings/7thmars2007/pdf/3325.pdf.

Kato, M., Sasaki, S., Tanaka, K., Iijima, Y., & Takizawa, Y. (2008). The Japanese lunar mission SELENE: Science goals and present status. Advances in Space Research, 42(2), 294-300. doi: 10.1016/j.asr.2007.03.049.

Kirchoff, M.R., Marchi, S., Bottke, W.F., Chapman, C.R. and Enke, B. (2021). Suggestion that recent (≤ 3 Ga) flux of kilometer and larger impactors in the Earth-Moon system has not been constant. Icarus, 355, p.114110. doi: 10.10.1016/j.icarus.2020.114110.

Kumar, P. S., Kumar, A. S., Keerthi, V., Goswami, J., Krishna, B. G., & Kumar, A. K. (2011). Chandrayaan-1 observation of distant secondary craters of Copernicus exhibiting central mound morphology: Evidence for low velocity clustered impacts on the Moon. Planetary and Space Science, 59(9), 870-879. doi: 10.1016/j.pss.2011.04.004.

Kenkmann, T., & Poelchau, M. H. (2009). Low-angle collision with Earth: the elliptical impact crater Matt Wilson, Northern Territory, Australia. Geology, 37(5), 459-462. doi: 10.1130/G25378A.1.

Lagain, A., Benedix, G.K., Servis, K., Baratoux, D., Doucet, L.S., Rajšic, A., Devillepoix, H.A.R., Bland, P.A., Towner, M.C., Sansom, E.K. and Miljković, K. (2021a). The Tharsis mantle source of depleted shergottites revealed by 90 million impact craters. Nature Communications, 12(1), p.6352. doi: 10.1038/s41467-021-26648-3.

Lagain, A., Bouley, S., Baratoux, D., Marmo, C., Costard, F., Delaa, O., Rossi, A.P., Minin, M., Benedix, G.K., Ciocco, M. and Bedos, B., (2021b). Mars Crater Database: A participative project for the classification of the morphological characteristics of large Martian craters. In Large Meteorite Impacts and Planetary Evolution VI, Reimold, W. U. and Koerbel, C. 10.1130/2021.2550(29). doi: 10.1130/2021.2550(29).

Lagain, A., Servis, K., Benedix, G.K., Norman, C., Anderson, S. and Bland, P.A. (2021c). Model age derivation of large Martian impact craters, using automatic crater counting methods. Earth and Space Science, 8(2), p.e2020EA001598. doi: 10.1029/2020EA001598.

Lagain, A., Devillepoix, H.A., Vernazza, P., Robertson, D., Granvik, M., Pokorny, P., Ozerov, A., Shober, P.M., Jorda, L., Servis, K. and Fairweather, J.H. (2024). Recalibration of the lunar chronology due to spatial cratering-rate variability. Icarus, 411, p.115956. doi: 10.1016/j.icarus.2024.115956.

LeCun, Y., Boser, B., Denker, J. S., Henderson, D., Howard, R. E., Hubbard, W., & Jackel, L. D. (1989). Backpropagation applied to handwritten zip code recognition. Neural computation, 1(4), 541-551. doi: 10.1162/neco.1989.1.4.541.

Le Feuvre, M. and Wieczorek, M.A. (2011). Nonuniform cratering of the Moon and a revised crater chronology of the inner Solar System. Icarus, 214(1), pp.1-20. doi: 10.1016/j.icarus.2011.03.010.

Marchi, S., Massironi, M., Cremonese, G., Martellato, E., Giacomini, L. and Prockter, L. (2011). The effects of the target material properties and layering on the crater chronology: The case of Raditladi and Rachmaninoff basins on Mercury. Planetary and Space Science, 59(15), pp.1968-1980. doi: 10.1016/j.pss.2011.06.007.

McEwen, A. S., & Bierhaus, E. B. (2006). The importance of secondary cratering to age constraints on planetary surfaces. Annu. Rev. Earth Planet. Sci., 34, 535-567. doi: 10.1146/annurev.earth.34.031405.125018.

McEwen, A. S., Preblich, B. S., Turtle, E. P., Artemieva, N. A., Golombek, M. P., Hurst, M., et al. (2005). The rayed crater Zunil and interpretations of small impact craters on Mars. Icarus, 176(2), 351-381. doi: 10.1016/j.icarus.2005.02.009.

Meyer Jr, C., Brett, R., Hubbard, N. a., Morrison, D., McKay, D., Aitken, F., et al. (1971). Mineralogy, chemistry, and origin of the KREEP component in soil samples from the Ocean of Storms. Paper presented at the Lunar and Planetary Science Conference Proceedings. doi: 10.1177/1474022206067628.

Michael, G., & Neukum, G. (2010). Planetary surface dating from crater size–frequency distribution measurements: Partial resurfacing events and statistical age uncertainty. Earth and Planetary Science Letters, 294(3-4), 223-229. doi: 10.1016/j.epsl.2009.12.041.

Michael, G.G., Platz, T., Kneissl, T. and Schmedemann, N. (2012). Planetary surface dating from crater size–frequency distribution measurements: Spatial randomness and clustering. Icarus, 218(1), pp.169-177. doi: 10.1016/j.icarus.2011.11.033.

Nagumo, K., & Nakamura, A. M. (2001). Reconsideration of crater size-frequency distribution on the moon: effect of projectile population and secondary craters. Advances in Space Research, 28(8), 1181-1186. doi: 10.1016/S0273-1177(01)00488-4.

Neukum, G., & Ivanov, B. (1994). Crater size distributions and impact probabilities on Earth from lunar, terrestrial-planet, and asteroid cratering data. Hazards due to Comets and Asteroids, 359(1), 359-416. https://api.semanticscholar.org/CorpusID:129481517.

Neukum, G., Ivanov, B. A., & Hartmann, W. K. (2001). Cratering records in the inner solar system in relation to the lunar reference system. Paper presented at the Chronology and Evolution of Mars: Proceedings of an ISSI Workshop, 10–14 April 2000, Bern, Switzerland. doi: 10.1023/A:1011989004263.

Neukum, G., König, B., & Arkani-Hamed, J. (1975). A study of lunar impact crater size-distributions. The Moon, 12(2), 201-229. doi: 10.1007/BF00577878.

Ohtake, M., Matsunaga, T., Haruyama, J., Yokota, Y., Morota, T., Honda, C., et al. (2009). The global distribution of pure anorthosite on the Moon. Nature, 461(7261), 236-240. doi: 10.1038/nature08317.

Osinski, G. R., Tornabene, L. L., & Grieve, R. A. (2011). Impact ejecta emplacement on terrestrial planets. Earth and Planetary Science Letters, 310(3-4), 167-181. doi: 10.1016/j.epsl.2011.08.012.

Robbins, S. J., & Hynek, B. M. (2014). The secondary crater population of Mars. Earth and Planetary Science Letters, 400, 66-76. doi: 10.1016/j.epsl.2014.05.005.

Robbins, S.J., Riggs, J.D., Weaver, B.P., Bierhaus, E.B., Chapman, C.R., Kirchoff, M.R., Singer, K.N. and Gaddis, L.R. (2018). Revised recommended methods for analyzing crater size‐frequency distributions. Meteoritics & Planetary Science, 53(4), pp.891-931. doi: 10.1111/maps.12990.

Salih, A. L., Lompart, A., Grumpe, A., Wöhler, C., & Hiesinger, H. (2017). Automatic Detection of Secondary Craters and Mapping of Planetary Surface Age Based on Lunar Orbital Images. International Archives of the Photogrammetry, Remote Sensing & Spatial Information Sciences, 42. doi: 10.5194/isprs-archives-XLII-3-W1-125-2017.

Schultz, P. H., & Singer, J. (1980). A comparison of secondary craters on the Moon, Mercury, and Mars. In: Pergamon Press.

Sharma, S., & Guleria, K. (2022). Deep learning models for image classification: comparison and applications. International Conference on Advance Computing and Innovative Technologies in Engineering, pp. 1733-1738. doi: 10.1109/ICACITE53722.2022.9823516.

Shoemaker, E., Batson, R., Bean, A., Conrad Jr, C., Dahlem, D., Goddard, E., et al. (1970). Preliminary geologic investigation of the Apollo 12 landing site: Part A: Geology of the Apollo 12 landing site.

Shoemaker, E. M., & Hackman, R. J. (1962). Stratigraphic basis for a lunar time scale. Paper presented at the The Moon. https://ser.im-ldi.com/MOON/IAU/shoemaker_hackman_1960.pdf.

Silver, L. (1971). U-Th-Pb isotope systems in Apollo 11 and 12 regolithic materials and a possible age for the Copernican impact. Eos Trans. AGU, 52, 534.

Singer, K. N., Jolliff, B. L., & McKinnon, W. B. (2020). Lunar secondary craters and estimated ejecta block sizes reveal a scale-dependent fragmentation trend. Journal of Geophysical Research: Planets, 125(8), e2019JE006313. doi: 10.1029/2019JE006313.

Stöffler, D., & Ryder, G. (2001). Stratigraphy and isotope ages of lunar geologic units: Chronological standard for the inner solar system. Paper presented at the Chronology and Evolution of Mars: Proceedings of an ISSI Workshop, 10–14 April 2000, Bern, Switzerland. doi: 10.1023/a:1011937020193.

Terada, K., Morota, T., & Kato, M. (2020). Asteroid shower on the Earth-Moon system immediately before the Cryogenian period revealed by KAGUYA. Nature Communications, 11(1), 3453. doi: 10.1038/s41467-020-17115-6.

Wang, N. and Zhou, J.L. (2016). Analytical formulation of lunar cratering asymmetries. Astronomy & Astrophysics, 594, p.A52. doi: 10.1051/0004-6361/201628598.

Wang Y., Zhuo M., & Zhang X. (2024). Automatic Crater Detection Tool for Moon, Mars, and Mercury (Version V6) [Data set]. Science Data Bank. doi:10.57760/sciencedb.11985.

Wilhelms, D., Oberbeck, V., & Aggarwal, H. (1978). Size-frequency distributions of primary and secondary lunar impact craters. Paper presented at the Lunar and Planetary Science Conference Proceedings.

Wilhelms, D.E., McCauley, J.F. and Trask, N.J., 1987. The geologic history of the Moon (No. 1348). doi: 10.3133/pp1348.

Williams, J.P., van der Bogert, C.H., Pathare, A.V., Michael, G.G., Kirchoff, M.R. and Hiesinger, H. (2018). Dating very young planetary surfaces from crater statistics: A review of issues and challenges. Meteoritics & Planetary Science, 53(4), pp.554-582. doi: 10.1111/maps.12924.

Xiao, Z. (2018). On the importance of self-secondaries. Geoscience Letters, 5(1), 17. doi: 10.1186/s40562-018-0116-9.

Xiao, Z., & Strom, R. G. (2012). Problems determining relative and absolute ages using the small crater population. Icarus, 220(1), 254-267. doi: 10.1016/j.icarus.2012.05.012.

Xiao, Z., Strom, R. G., Chapman, C. R., Head, J. W., Klimczak, C., Ostrach, L. R., et al. (2014). Comparisons of fresh complex impact craters on Mercury and the Moon: Implications for controlling factors in impact excavation processes. Icarus, 228, 260-275. doi: 10.1016/j.icarus.2013.10.002.

Yue, Z., Johnson, B.C., Minton, D.A., Melosh, H.J., Di, K., Hu, W. and Liu, Y. (2013). Projectile remnants in central peaks of lunar impact craters. Nature Geoscience, 6(6), pp.435-437. doi: 10.1038/ngeo1828.

Zhuo, M., Wang, Y., (2024). Secondary and primary craters in and around the Copernicus crater[DS/OL]. V7. Science Data Bank, doi:10.57760/sciencedb.16270.

Zhuo, M., Wang, Y., Zhang X. & Chen, Z. (2025) High-Accuracy Crater Detection for Complex Planetary Surfaces. IEEE Transactions on Geoscience and Remote Sensing, vol. 63, pp. 1-14. doi: 10.1109/TGRS.2025.3560283.